www.sciencemag.org/cgi/content/full/316/5827/1026/DC1

# Supporting Online Material for

## Stress Control of Deep Rift Intrusion at Mauna Loa Volcano, Hawaii

Falk Amelung,* Sang-Ho Yun, Thomas R. Walter, Paul Segall, Sang-Wan Kim

*To whom correspondence should be addressed. E-mail: famelung@rsmas.miami.edu

Published 18 May 2007, *Science* **316**, 1026 (2007)
DOI: 10.1126/science.1140035

**This PDF file includes:**

Materials and Methods
Table S1
Figs. S1 to S4
References

## Supporting Online Material

## Material and Methods

### Uniform excess pressure dike model

We assume that uniform excess pressure acts everywhere on the wall of the magma body, with no shear traction. This uniform-pressure boundary condition is physically more plausible than a kinematic displacement boundary condition if we can assume that low-viscous fluid such as basaltic magma is at hydrostatic (or magmastatic) pressure equilibrium. Magma at depth migrates commonly in the form of a crack. We divide the crack into elements that either open or remained closed. The open elements define the geometry of the crack. The uniform pressure boundary condition is enforced on all the open elements. In an inversion various combinations of open and closed elements are selected, and for each combination (i.e. crack geometry), the opening distribution of the entire crack is uniquely determined by a boundary element calculation under the uniform excess pressure (*1*).

Figure S1 shows an example of this procedure. The crack (dike or sill) plane is divided into many dislocation elements (Fig. S1A), and then open elements, which are indicated as white, are randomly selected (Fig. S1B). A uniform excess pressure is then applied to those open elements and the amount of opening at each element is calculated using a boundary element method (Fig. S1C). The red color indicates large opening, and the blue color means small opening. Note that under a uniform pressure isolated open elements have small openings and connected open elements achieve large openings, because the connected elements constitute a more compliant crack than the isolated elements.

Given the pattern of the open elements and their associated openings, we use a Green's function in an elastic half-space to simulate the surface deformation. The surface deformation is then projected onto the line-of-sight unit vectors to produce a set of model predictions (i.e. simulated interferograms). These model predictions are compared with observed interferograms, and the objective of our inversion is to find an optimal pattern of the open elements that minimizes the difference between the simulated and observed interferograms. The best-fit combination of the binary parameters that represents the pattern of

the open elements is searched with simulated annealing method (*2*) that applies Basu and Frazer type rapid determination of the critical temperature (*3*).

Compared to kinematic inversion, this approach has smaller number of degrees of freedom, as there is only one unique solution for the openings for a given combination of the binary parameters. No smoothing constraints are needed to assure smoothly varying opening distribution. The uniform pressure boundary condition guarantees smooth crack opening distribution. The opening distribution determined by the physical boundary condition produces more realistic stress field in the host rock than a kinematic model, where opening distribution is subject to non-physical smoothing constraints. See (*4*) for a more detailed description of the modeling approach.

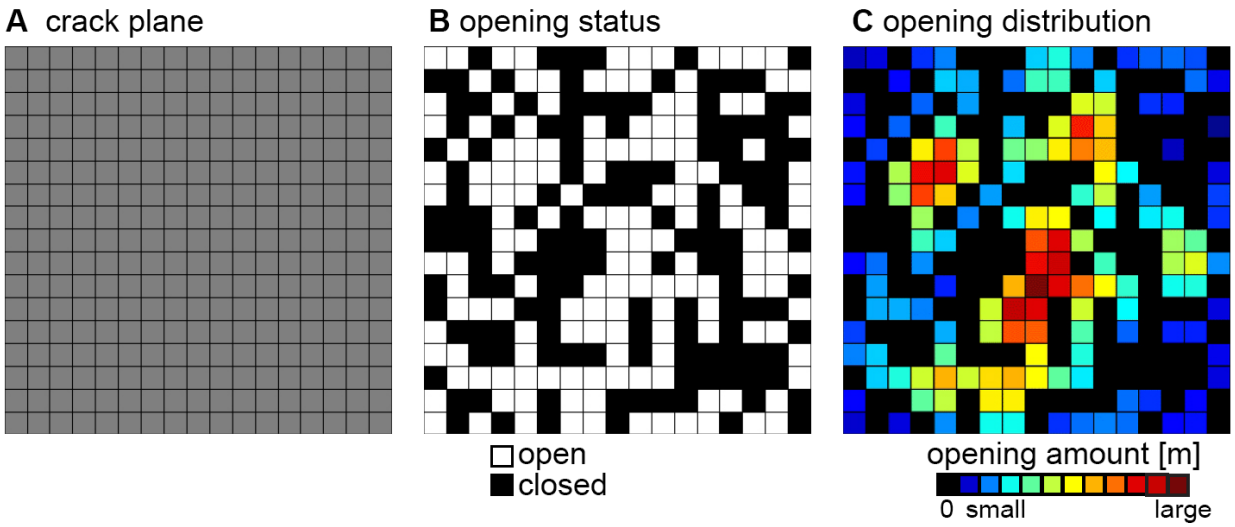


**Figure S1**. Example model geometry of the binary parameter inversion. (a) Subdivided crack plane where many dislocation elements are defined. (b) Open (white) and closed (black) elements represented by a combination of binary parameters. (c) The amount of opening calculated at each element subject to a uniform excess pressure.

| Radar imaging beam | Date1-Date2 | $B_{perp}$ [m] |
|---|---|---|
| Descending 1 | 2001 03 06 - 2005 10 11 | 119.4 |
| | 2001 04 23 - 2005 11 04 | -90.7 |
| | 2001 05 17 - 2005 11 28 | 67.9 |
| | 2001 08 21 - 2005 09 17 | -132.7 |
| | 2001 11 01 - 2005 08 24 | -79.5 |
| | 2002 01 12 - 2006 01 15 | 182.1 |
| | 2002 05 12 - 2005 06 13 | -437.2 |
| | 2002 07 23 - 2005 07 07 | 457.6 |
| Descending 6 | 2001 01 14 - 2005 11 01 | 363.4 |
| | 2001 03 03 - 2005 03 06 | 406.5 |
| | 2001 07 01 - 2005 09 14 | 129.9 |
| | 2001 08 18 - 2005 08 21 | 229.0 |
| | 2001 12 16 - 2005 03 30 | 388.9 |
| | 2002 06 02 - 2005 12 19 | 790.8 |
| | 2002 06 26 - 2005 07 28 | -48.2 |
| | 2002 07 20 - 2005 11 25 | -243.8 |
| Ascending 3 | 2001 04 22 - 2006 01 14 | 378.2 |
| | 2001 05 16 - 2005 02 12 | 34.2 |
| | 2001 06 09 - 2006 03 27 | -325.9 |
| | 2001 08 20 - 2005 08 23 | -157.0 |
| | 2001 10 07 - 2005 11 03 | -421.0 |
| | 2001 10 31 - 2005 03 08 | 35.2 |
| | 2002 02 04 - 2005 12 21 | -159.6 |
| | 2002 04 17 - 2006 02 07 | -268.6 |
| | 2002 09 08 - 2005 11 27 | -9.3 |
| Ascending 6 | 2001 09 23 - 2005 08 09 | 551.5 |
| | 2002 01 21 - 2005 06 22 | 558.3 |
| | 2002 03 10 - 2005 12 07 | 349.3 |
| | 2002 04 03 - 2005 10 20 | 44.9 |
| | 2002 05 21 - 2005 07 16 | 756.5 |

**Table S1.** SAR interferograms used to obtain averaged LOS velocities for the four different viewing geometries. Radar imaging beam stands for the viewing geometry, Date1, Date2 are the dates of the images for each interferogram, and $\mathbf{B}_{perp}$ is the perpendicular baseline separation between the satellite orbits during image acquisition. Descending, satellite traveling south, ascending, satellite traveling north; all imagery is in Standard beam modes with the mode number given. The Radarsat acquired a total of 450 SAR images of Hawaii during 1997-2005.

For all of the 4 viewing geometries we formed all possible interferograms covering the 2002-2005 inflation period and selected the interferograms with smallest atmospheric and residual orbital phase contributions which we averaged to obtain mean LOS velocity fields. The averaged rates for the different viewing geometries are for slightly different time spans because of the different time periods covered by the interferograms (3.41, 3.30, 3.37 and 3.26 years for Standard Beams A3, A6, D1 and D6, respectively).

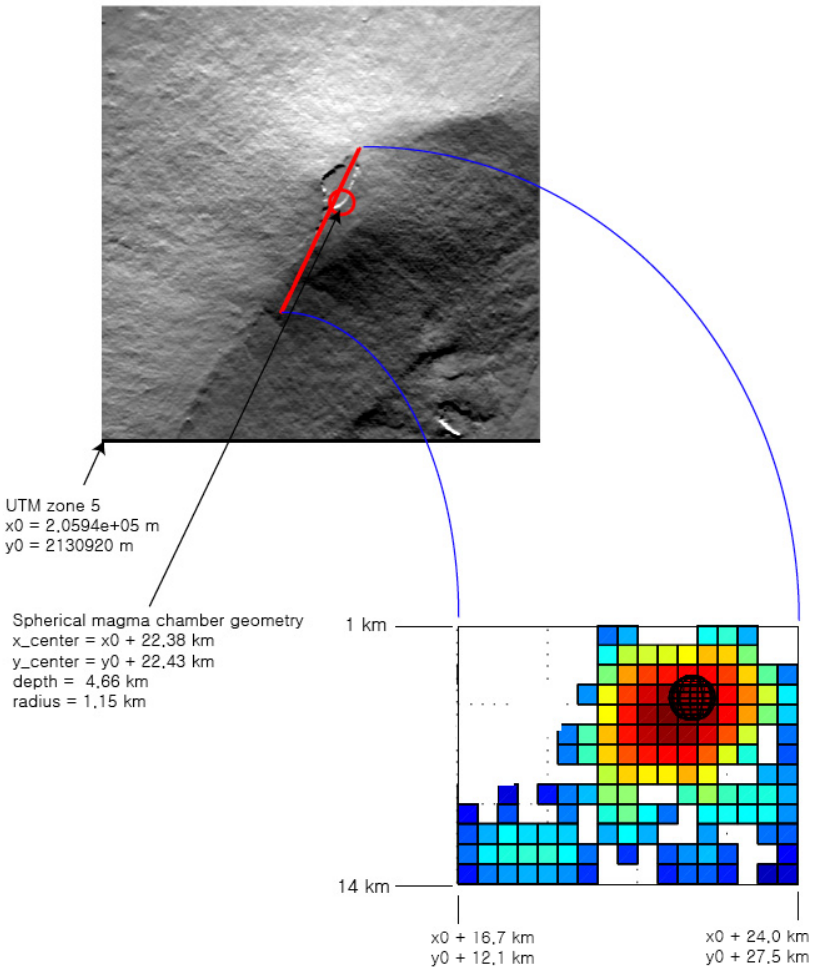


**Figure S2.** Model geometry. Coordinates of the magma chamber center and of the dike in km relative to the lower left corner of the map inset for which the UTM coordinates are given.

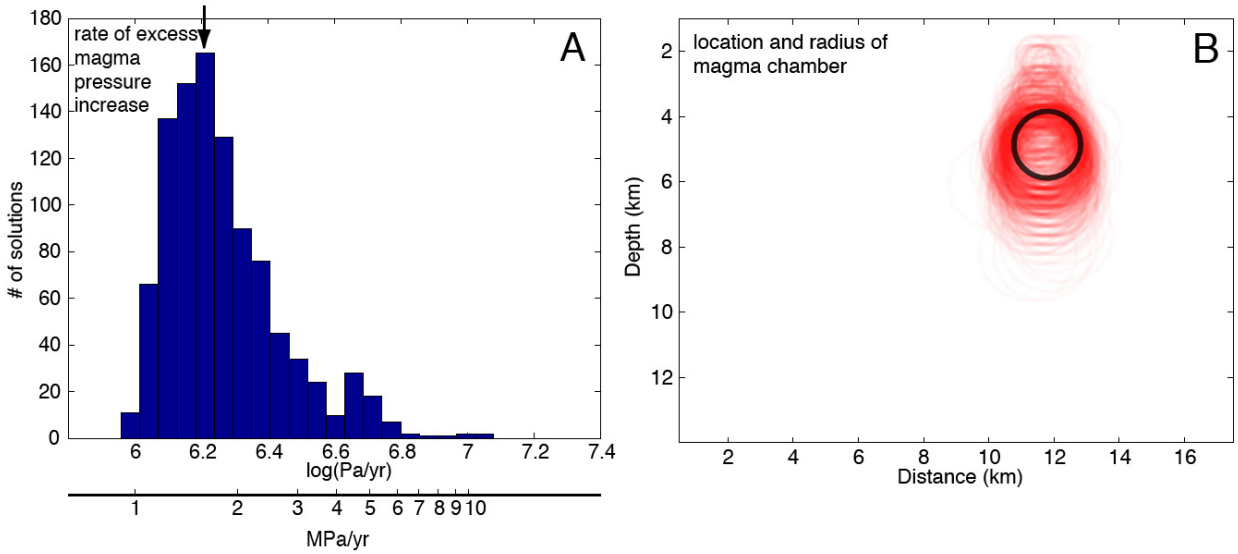


**Figure S3:** Pseudo-probability density distributions for some of the inferred model parameters. **A** rate of excess magma pressure increase. **B** magma chamber geometry. The distributions have been obtained by running the simulating annealing inversion 20 times and taking for each run the 50 best-fitting samples. We call them pseudo-probability densities because of the simplified sampling method from the model space which does not yield actual probabilities. The pseudo-probability density distribution for the excess magma pressure rate is shown in form of a histogram (binned in a logarithmic scale). The pseudo-probability density distribution for the magma chamber geometry is shown in form of a cloud of circles, each describing the location along the rift, depth, and radius of a sample. The minimum misfit solution is shown by a black arrow and black circle in A and B, respectively. We define as pseudo-95% confidence intervals the ranges of the model parameters containing 95% of the samples. The pseudo 95%-confidence intervals are 1.2-3.1 MPa/yr for the rate of excess magma pressure, 3.5-7 km for the chamber depth and 0.8-1.3 km for the chamber radius.

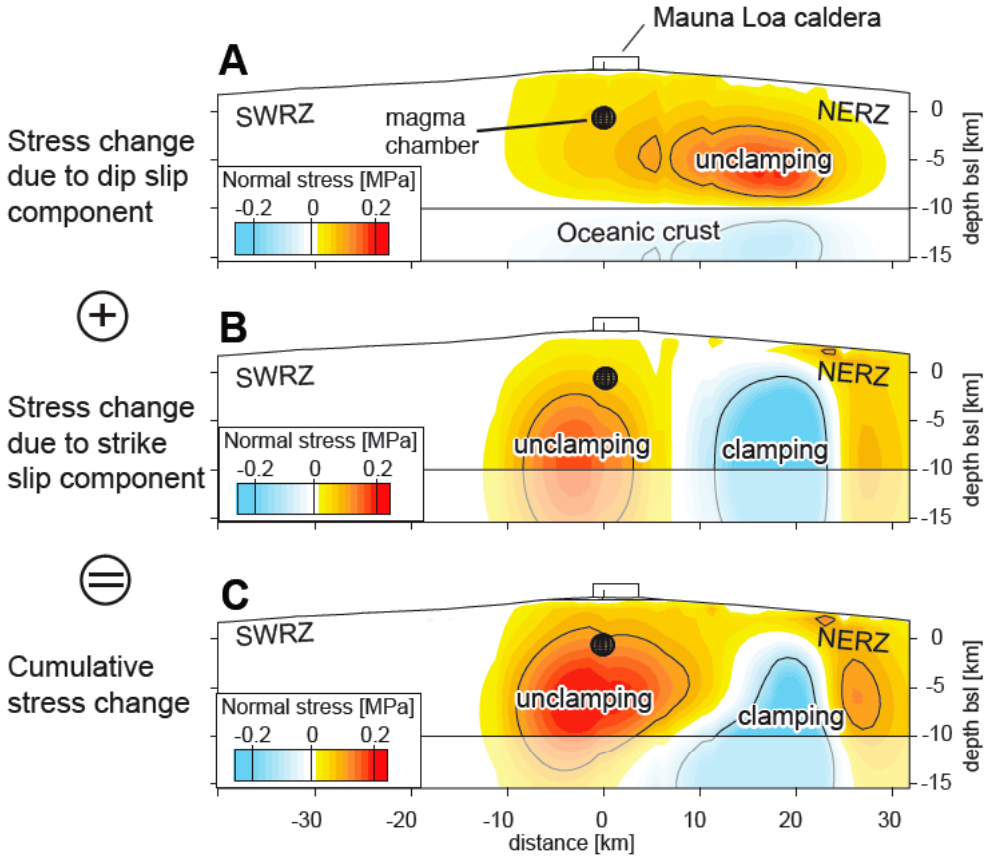


**Figure S4:** Change in normal stress along the rift zone due to the M6.6 1983 Kaoiki earthquake. A due to the dip-slip component. B, due to the strike-slip component and C the sum of A and B as in Fig 3A

We model the earthquake by an equal amount of strike slip along a vertical fault and seaward slip along a 5° inward-dipping decollement fault, in the Kaoiki area located at about 9 km below sea level, each with a slip of 0.35 m along a 240 km$^2$ fault surface corresponding to earthquakes with moment magnitude 6.4. We use the fault geometry is described by (*5*). A combined strike-slip and decollement-slip earthquake on two different faults is consistent with seismology. The first-motion and body-wave focal mechanism indicate right-lateral strike-slip along a vertical fault (*6*); the existence of such faults has been confirmed by precise earthquake relocations (*7*). The surface-wave derived moment tensor indicates predominantly decollement-type thrust slip (*8-10*). A possible explanation is that the earthquake originated as a strike-slip event and continued as a decollment earthquake (*11*). B shows that the strike-slip component is responsible for the stress changes promoting the 2002-2005 intrusion.

## References


S1. S. Yun, P. Segall, H. Zebker, *J. Volc. Geotherm. Res.* **150**, 232 (2006).
S2. P. Cervelli, M. H. Murray, P. Segall, Y. Aoki, T. Kato, *J. Geophys. Res.* **106**, 11217 (2001).
S3. A. Basu, L. N. Frazer, *Science* **249**, 1409 (1990).
S4. S.-H. Yun, *Thesis, Stanford University* (2007).
S5. T. R. Walter, F. Amelung, *J. Geophys. Res.* **111** (2006).
S6. M. D. Jackson, E. T. Endo, P. T. Delaney, T. Arnadottir, A. M. Rubin, *J. Geophys. Res.* **97**, 8775 (1992).
S7. J.-L. Got, P. Okubo, *J. Geophy. Res.* **108** (2003).
S8. R. Y. Koyanagi *et al.*, *U.S. Geol. Surv. Open-File Rep. 84-798* (1984).
S9. E. T. Endo, Thesis, University of Washington (1985).
S10. S. A. Sipkin, *Phys. Earth Planet. Int.* **47** (1987).
S11. T. R. Walter, F. Amelung, *Geophys. Res. Lett.* **31** (2004).